NEAR-FIELD DYNAMICS OF A TURBULENT ROUND JET WITH MODERATE SWIRL

Luca Facciolo, P. Henrik Alfredsson
Linné Flow Centre, KTH Mechanics,
Royal Institute of Technology,
S-100 44 Stockholm, Sweden
facciolo@mech.kth.se, hal@mech.kth.se

Yvan Maciel
Department of Mechanical Engineering,
Laval University
Quebec City, G1K 7P4, Canada
ymaciel@gmc.ulaval.ca

ABSTRACT

The near-field characteristics of a turbulent jet with moderate swirl generated by a fully developed, axially rotating pipe flow are investigated with LDV and time resolved stereoscopic PIV measurements. Of special interest is the newly discovered counter-rotating core which develops about six jet diameters downstream the jet exit. Measurements of all six Reynolds stresses are reported at this position and it is argued that the counter rotation is the result of the transport of angular momentum from the core region towards the outer regions by the radial-azimuthal Reynolds shear stress. The mechanisms behind this transport are discussed by qualitative analysis of the time resolved PIV data and comparisons with the non-swirling case are made.

INTRODUCTION

In a turbulent round jet, the presence of swirl may strongly affect the mean flow features. At swirl ratios above a critical level so called vortex breakdown occurs which completely changes the jet behaviour. At moderate swirl numbers, i.e. swirl numbers below the onset of vortex breakdown, the turbulence and spreading of the jet increase. In the following we will limit ourselves to moderate swirl for which vortex breakdown does not occur. A swirling round jet is axi-symmetric on average but the swirl breaks the symmetry, which means that the two Reynolds shear stresses which involve the fluctuating azimuthal component are non-zero in contrast to the non-swirling case.

For both non-swirling and swirling jets, initial conditions are known to have a strong influence on the downstream development of the jet. The structure of the near-field turbulence is distinctly different between a jet exiting from a smooth contraction nozzle with a thin laminar shear layer and a jet exiting from a long pipe with a fully developed turbulent pipe flow profile. In the case of the pipe jet flow, the regular formation of vortex rings resulting from the shear layer instability is disrupted by turbulent exit conditions (Mi et al. 2001, Xu and Antonia 2002). Xu and Antonia (2002) showed that the initially thicker shear layer in the case of the pipe jet flow results in longer wavelength primary instabilities and structures. Mi et al. (2001) provide some evidence that the formation of large-scale structures in the pipe jet occurs much farther downstream (around six jet diameters) than in the contraction jet (around one jet diameter).

The situation becomes even more complicated when swirl is added since many swirl-generating mechanisms have been used, such as guide vanes, rotating honeycombs, transverse injection etc. The resulting flow is to a certain extent dependent on the geometrical details of the apparatus, which makes comparisons between various studies difficult. One method to get an apparatus-independent swirl is to use an axially rotating, fully developed pipe flow as the source for the swirling jet. Such a pipe flow apparatus was developed by Facciolo (2006). However it was discovered (Facciolo et al. 2007) that the resulting swirling jet flow has a puzzling characteristic, namely that at approximately six pipe diameters downstream of the pipe outlet, the jet core starts to rotate (albeit at a low rate) in the opposite direction as compared to the rotation of the pipe. Our aim in this paper is to further investigate this behaviour using LDV and PIV measurement techniques.

EXPERIMENTAL METHODS

Pipe flow apparatus

The jet flow is generated from a fully developed turbulent pipe flow for both the swirling and non-swirling cases. The pipe has a length of 6 m and a diameter D of 60 mm. The pipe can be rotated along its axis with a maximum rotation rate of 30 rev/s. The flow is entering the ambient still air through a large non-rotating plate (for more details see Facciolo, 2006).

A laboratory-fixed cylindrical reference frame is used to describe the flow. We denote the radial, azimuthal and axial directions by r, θ and x with the origin of the coordinate system at the centre of the pipe outlet. The corresponding velocity components are u_r, u_θ and u respectively. For convenience, a cartesian reference frame is also defined with y in the horizontal direction and z in the vertical direction, and corresponding velocity components v and w.

LDV-systems

Two different LDV systems were used. The first one is a FlowLite system from DANTEC used to measure the streamwise and azimuthal velocity components separately. The system comprised of a backscatter fibre optics probe with a beam expander, a Bragg cell and a signal analyser of correlation type. The light source was a 10 mW He-Ne laser.

The measuring volume, an ellipsoid, had the dimensions: 0.81×0.09×0.09 mm^3. The data rate varied depending on the measurement position with the highest rate in the central region. To acquire statistically independent samples the sampling rate was limited to 100 Hz (estimated as U_b/D, where U_b is the bulk velocity in the pipe and D is the pipe inner diameter). The sampling was stopped either at 12000 samples or after 240 s.

The second LDV system, an Aerometric optical system, was used to measure the radial and azimuthal components. Here an Argon laser, with wave lengths of 488 and 514 nm, together with Bragg cells, was used. The signals were analyzed using a two channel BSA Flow system from DANTEC. The optical axes of the LDV probes are perpendicular to each other to allow simultaneous measurements of the radial and azimuthal velocity components. In order to minimize the probe volume (which for each probe is similar to the one of the FlowLite system), the scattered light was picked up by the probe head at 90° to the one emitting the light, thereby effectively reducing the probe volume to a sphere with a diameter of 0.1 mm. Data were only acquired when simultaneous signals were coming from both probes showing that the same particle is giving rise to both signals. For this set of measurements, the number of independent samples was typically around 20000.

The particles used for the LDV measurements are small droplets of condensed smoke of polyethylenglycol. They are injected into the air at the inlet of the centrifugal fan.

PIV system

The stereoscopic PIV system consists of two high speed digital cameras Photron Fastcam APX RS, CMOS sensor, which can catch images up to 250 kHz, and a dual-head, high-repetition-rate, diode-pumped Nd:YLF laser Pegasus PIV by New Wave with a maximum frequency of 10 kHz. During the experiments the image pairs are captured at a frequency of 1.5 kHz with a resolution of 1024×1024 pixels at 10 bit using Nikon Nikkor 105 mm lenses. Two types of datasets were obtained. The first one corresponds to measurements over a long time period ($1.4 \times 10^4 D/U_b$) in order to perform statistics with statistically independent velocity field realizations (generally 3696 realizations). The second type consists in time-resolved measurements with a temporal resolution of $0.077D/U_b$ and typically 3072 realizations. For both types of datasets, the spatial resolution is approximately $0.015D$.

A commercial software from La Vision (Davis 7.0) has been used for the stereoscopic calibration and the processing of the images. In stereo PIV, important systematic errors can be introduced by slight misalignments of the laser sheet with respect to the calibration plane. These errors were reduced by applying a self-calibration procedure available in Davis 7.0. The remaining systematic errors were still too large in relative terms for the components v and w in the yz-planes. In order to have reliable strain and rotation rates when analysing the instantaneous velocity fields, a procedure was used to correct the remaining systematic errors for the components v, w, u_r and u_θ by using the LDV mean data as reference data. The fields are also corrected for small geometric misalignment errors of the measurement plane. A two-dimensional homogeneous Gaussian filter is finally used to smooth the raw instantaneous PIV velocity fields. The size of the spatial filtering window is 5×5 grid points.

The seeding used for the PIV is the same as for the LDV, with the difference that the droplets of polyethylenglycol are generated by an atomiser which makes them larger and thereby peak locking problems in the images are avoided.

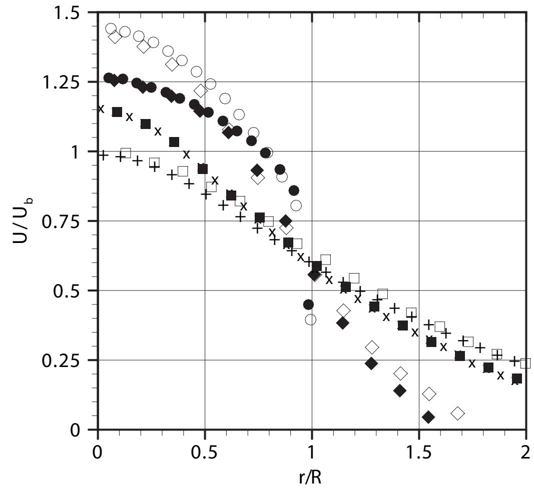

Figure 1: Mean axial velocity profiles. LDV: (○) $x/D = 0$, (◇) $x/D = 2$, (□) $x/D = 6$, open symbols $S = 0.47$, filled symbols $S = 0$. PIV: $x/D = 6$, (+) $S = 0.43$, (×) $S = 0$.

RESULTS AND DISCUSSION

All the data presented here is for $Re = U_b D/\nu \approx 24000$ and swirl numbers of $S = 0$ and $S \approx 0.5$ ($S = 0.47$ for the LDV measurements and 0.43 for the PIV ones). The swirl number is defined as $S = V_w/U_b$ where V_w is the azimuthal velocity of the inner pipe wall. Comparisons between the LDV and PIV data are presented at $x/D = 6$, where data from both measurement systems are available. The PIV profiles shown here were all obtained by averaging the data of the planar fields in the azimuthal direction. In the case of the LDV data, the profiles presented are the average of the lower and upper half-profiles. Complete profiles have already been presented in Facciolo et al. (2007) and they reveal a good symmetry of the data.

Mean velocity

The LDV data is used first to present the streamwise evolution of the mean flow characteristics. The mean axial velocity profiles at three streamwise positions with and without swirl are shown in Fig. 1. The initial profile at the pipe outlet is more peaked for the swirling flow case. However, further downstream at $x/D = 6$ the axial velocity in the central region becomes significantly smaller than in the non-rotating case. At the latter position, it is seen that the LDV and PIV data agree well.

Figure 2 shows the downstream evolution of the mean azimuthal velocity profiles (U_θ/V_w) for the swirling jet. The velocity profile at the pipe outlet closely follows a profile proportional to $(r/R)^2$ (curved line). Note that the straight line corresponds to solid body rotation while the lines in the small frame are polynomial fits for visual aid. From the figure it is seen that the maximum of U_θ decreases to almost 50% of the pipe wall velocity in only one diameter, due to the entrainment of ambiant fluid. At $x/D = 8$, the maximum of U_θ is reduced to about 10% of V_w and is shifted to $r/R \approx 2$.

The smaller frame in Fig. 2 shows a close-up of the profiles in the central region of the jet. As can be noted, the LDV data in the entrance region lay on a single curve (close to a parabolic curve) until $x/D = 3$. At $x/D = 5$ the azimuthal velocity has significantly decreased but the profile is still monotonic. However at $x/D = 6$ the profile reveals a

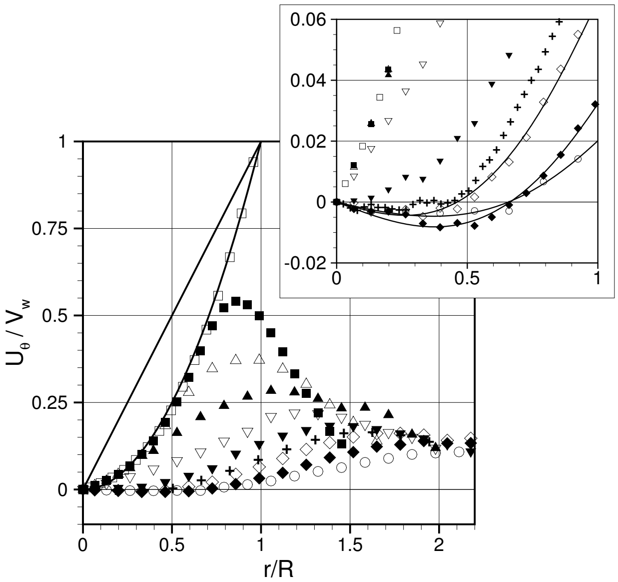

Figure 2: Mean azimuthal velocity profiles of the swirling jet. LDV: (□) x/D=0, (■) x/D=1, (△) x/D=2, (▲) x/D=3, (▽) x/D=4, (▼) x/D=5, (◇) x/D=6, (◆) x/D=7, (○) x/D=8. PIV: (+) x/D=6. Small frame: close up in jet core. Not all data points shown for clarity.

change in sign meaning that in average the jet, in the central region, rotates in a direction which is opposite to that imposed by the rotating pipe. The azimuthal velocity of the counter rotating core is fairly small, about 1% of V_w, and it covers a region slightly smaller than the pipe diameter. The counter rotating region starts between $5D$ and $6D$ downstream of the pipe outlet, increasing in magnitude and reaching a maximum between $6D$ and $8D$.

The comparison in Fig. 2 between the PIV and LDV U_θ-profiles at $x/D = 6$ reveals a fairly good agreement. Note however that such an agreement is reached only when the PIV data is averaged over the azimuthal direction. Relatively large systematic errors of U_r and U_θ exist for the PIV data due to the misalignment problems described in the previous section. Since U_r and U_θ are very small at $x/D = 6$, the errors reach $\pm 30\%$ of its maximum value for U_θ and $\pm 100\%$ of its maximum value for U_r. As mentioned previously, a procedure was used to correct the PIV instantaneous velocity data for these systematic errors.

Reynolds stresses

Figure 3 shows the radial distribution of the Reynolds normal stresses at $x/D = 6$ for both non-swirling and swirling cases obtained from the PIV measurements. Also included are the LDV measurements for the cross stream components in the swirling case. For all stresses the level is higher in the swirling case (typically 50–100% higher values) as compared to the non-swirling case. In the swirling case we can note that the stresses in the core region are fairly constant, whereas for the non-rotating case the stresses have a maxima around $r/R = 0.8$. We can also note that there is a good correspondence between the LDV and the PIV data.

In axisymmetric non-swirling jets, only one of the the Reynolds shear stresses, namely $\overline{u'u'_r}$, is different from zero, whereas the other two stresses are zero due to symmetry. In figure 4 all the Reynolds shear stresses are shown (except those which are zero by definition). Also here it is clear that in the non-swirling case the $\overline{u'u'_r}$ stress is at a lower level

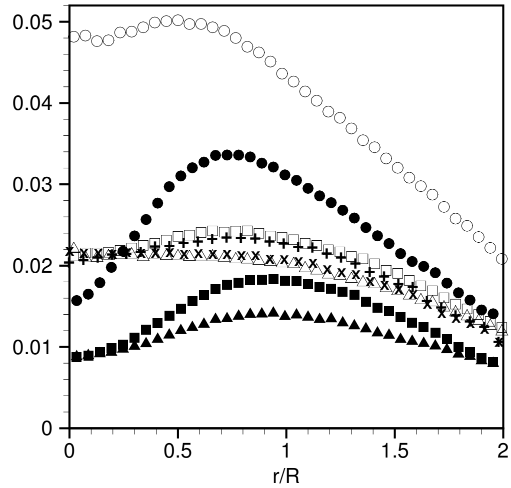

Figure 3: Reynolds normal stress profiles at $x/D = 6$ normalized with U_b. PIV: (○) $\overline{u'^2}$, (□) $\overline{u_\theta'^2}$, (△) $\overline{u_r'^2}$, open symbols $S = 0.43$, filled symbols $S = 0$. LDV, $S = 0.47$: (+) $\overline{u_\theta'^2}$, (×) $\overline{u_r'^2}$.

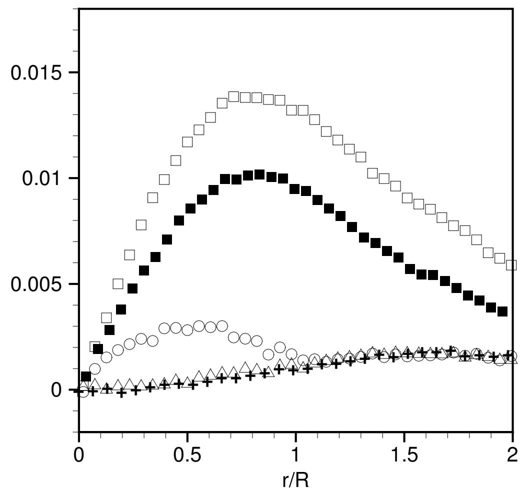

Figure 4: Reynolds shear stress profiles at $x/D = 6$ normalized with U_b. PIV: (○) $\overline{u'u'_\theta}$, (□) $\overline{u'u'_r}$, (△) $\overline{u'_\theta u'_r}$, open symbols $S = 0.43$, filled symbols $S = 0$. LDV, $S = 0.47$: (+) $\overline{u'_\theta u'_r}$.

than for the swirling case. More interesting is to see the distribution of the two other stresses which both are positive. An interesting feature is the local maximum of $\overline{u'u'_\theta}$ around $r/R = 0.5$. The comparison for $\overline{u'_\theta u'_r}$ between the PIV and the LDV measurements is also fairly convincing.

Mean angular momentum

It is possible to formulate an approximate conservation equation for the axial flux of angular momentum which states

$$\frac{d}{dx}\int_0^\infty \rho(U\Gamma + r\overline{u'u'_\theta})2\pi r dr = 0$$

where ρ is the density and $\rho\Gamma = \rho r U_\theta$ can be viewed as the mean angular momentum density. With this in mind it is of interest to investigate how the transport budget for Γ is balanced within the yz-plane in order to shed some light on the occurence of the counter-rotating core. A balance equation for Γ, (if we neglect viscous diffusion and $\partial\overline{u'u'_\theta}/\partial x$) can be

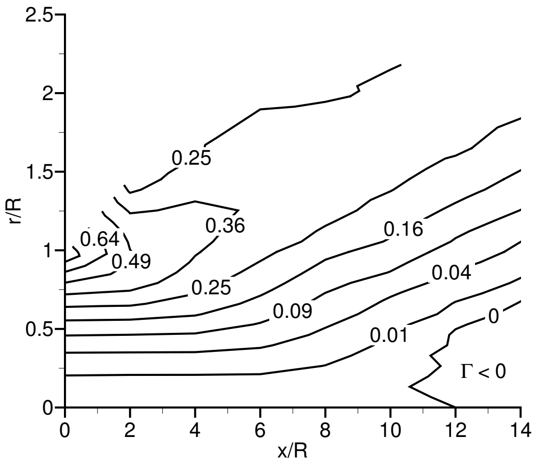

Figure 5: Contours of mean angular momentum density. The contour levels are non-uniformly spaced as a function of $(\Gamma/(RV_w))^2$.

written as

$$U\frac{\partial\Gamma}{\partial x}+U_r\frac{\partial\Gamma}{\partial r}+\frac{1}{r}\frac{\partial}{\partial r}(r^2\overline{u'_\theta u'_r})=0 \qquad (1)$$

The first two terms are streamwise and radial advection of Γ respectively, whereas the last term is transport through the cross stream Reynolds shear stress. We use the LDV data to analyze the different terms in this equation. The radial and streamwise variation of $\Gamma/(RV_w)$ is depicted in Fig. 5. Γ spreads radially outward very fast as it is advected downstream. It is apparent from Fig. 5 that the core of the jet (say $r/R < 0.5$) is a region of very low mean angular momentum and the latter keeps decreasing downstream until it eventually changes sign.

In the swirling jet, turbulence is efficient in transporting angular momentum radially outwards. Moreover, because the Reynolds shear stress $\overline{u'_\theta u'_r}$ is greater or equal to zero for all radial positions (Fig. 4), radial turbulent transport of Γ is directed outwards everywhere in the jet.

Consider an infinitesimal control volume (ICV) in the jet. A gain (loss) of Γ in the ICV is represented by a term of negative (positive) value in Eq. 1. Figure 6 presents a budget of Γ at $x/D = 6$, a position where a counter-rotating core is present roughly between $r/R = 0$ and 0.5. In the region represented in Fig. 6, streamwise advection leads everywhere to a gain of Γ in an ICV, while radial turbulent transport leads to a loss of Γ. Note that further outwards, radial turbulent transport has to eventually correspond to a gain since:

$$\frac{\partial}{\partial r}(r^2\overline{u'_\theta u'_r})<0 \text{ for large } r \qquad (2)$$

As can be seen in Fig. 6 the balance is not fulfilled in the outer part mainly because of the high uncertainties in $\partial\Gamma/\partial x$. The Γ data is too far apart in the streamwise direction to capture accurately the variations of Γ in the jet outer part.

Figure 7 presents the same budget but now only in the core region. In this region, the loss of Γ due to turbulent transport is greater than the gain due to streamwise advection. Consequently, radial advection of Γ becomes negative (gain of Γ) while it was always positive upstream. The core region therefore starts to counter-rotate since

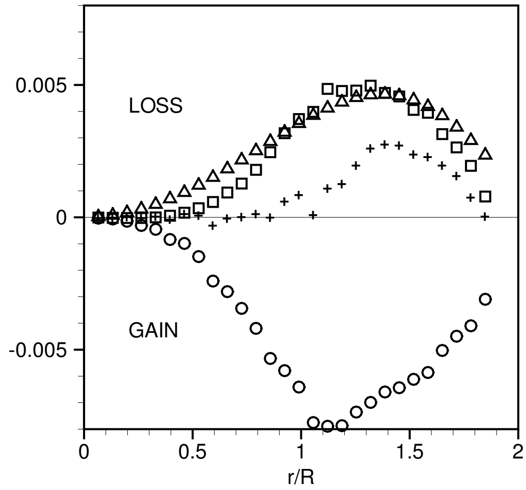

Figure 6: Budget of mean angular momentum density at $x/D = 6$. The terms are normalized with R and U_b. Streamwise advection (○), radial advection (□), radial turbulent transport (△), sum of all the terms (+).

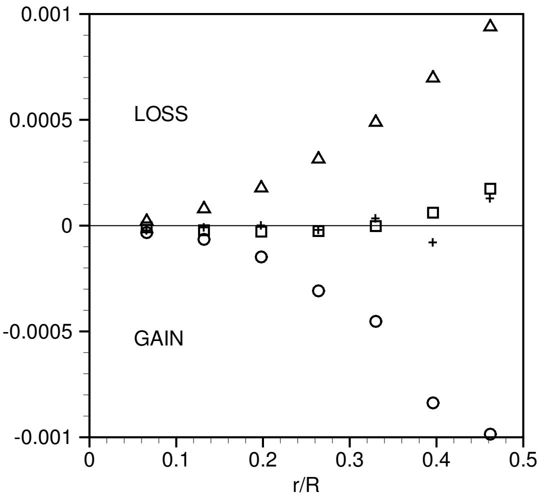

Figure 7: Budget of mean angular momentum density in the core region at $x/D = 6$. Symbols as in Fig. 6.

$$U_r\frac{\partial\Gamma}{\partial r}<0 \Rightarrow \frac{\partial U_\theta}{\partial r}<0 \Rightarrow U_\theta<0 \quad (U_\theta=0 \text{ at } r=0) \qquad (3)$$

If the swirling jet was laminar, streamwise and radial advections would always balance each other and counter-rotation would be impossible. Counter-rotation exists in a turbulent swirling jet because of the strong radial turbulent transport of mean angular momentum. If this also occurs in swirling jets which are generated in a different manner is at present an open question.

Instantaneous fields

By analysing the time and space resolved data from the stereoscopic PIV it is possible to capture the evolution of the flow and its structures. The figures presented next form a very limited selection of snapshots (combined vector/contour plots) taken from the long sequences of time resolved data. The discussion below is based on viewing videos of these and other plots that each cover two seconds of recording.

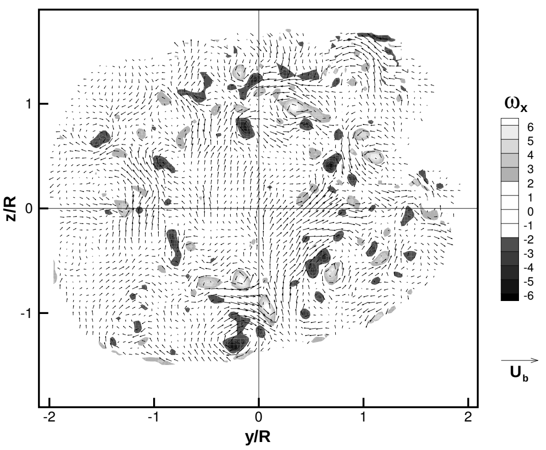

Figure 8: Instantaneous velocity field at $x/D = 6$ and contours of streamwise vorticity. $S = 0$. Only one vector out of 4 is shown for clarity.

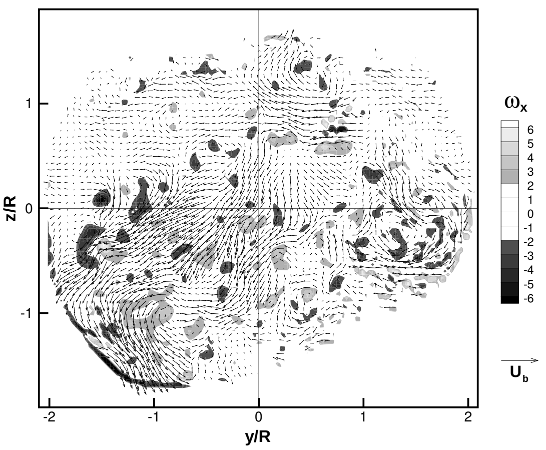

Figure 9: Instantaneous velocity field at $x/D = 6$ and contours of streamwise vorticity. $S = 0.43$. Only one vector out of 4 is shown for clarity.

Clearly the first impression from viewing the videos in the yz-plane is that the swirling jet contains more violent large-scale motions than the non-swirling jet. A comparison of the v-w vector plots at $x/D = 6$ shown in Figs. 8 and 9 gives an idea of this difference. Large sweeping motions are frequent in the swirling jet while they do not occur at such a scale and strength in the non-swirling jet. Such motions appear frequently in the form of coherent bands (in the yz-plane) the size of the jet diameter. As a result, the side views of the flow (xz-plane) show quite frequently large vertical bands of v of the same sign, as seen in Fig. 10. Note that U_θ is everywhere smaller than $0.07U_b$ at $x/D = 6$. The mean swirling motion is therefore small compared to the sweeping motions shown in Figs. 9 and 10.

For the particular case shown in Fig 10, the v-sweeping motions are also accompanied by a waviness of the jet as seen with the contours of u in Fig. 11. Such jet waviness with a wavelength in the order of two jet diameters is recurrent but it alternates with periods where the jet remains fairly straight. The waviness was not found (with the videos of the u-contours in the yz-plane) to be linked to a helical motion of the jet. The jet rather rapidly meanders and changes shape

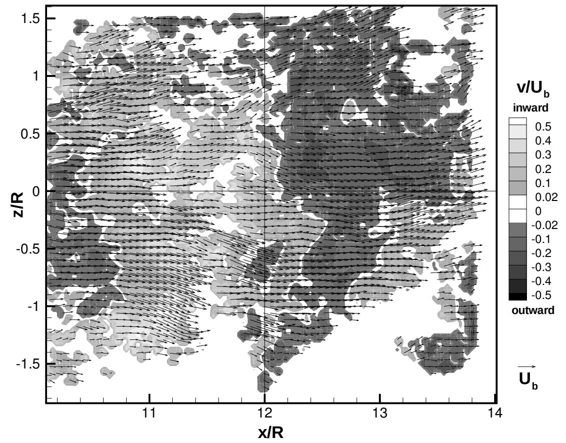

Figure 10: Instantaneous velocity field in xz-plane at $y = 0$ and contours of v. $S = 0.43$.

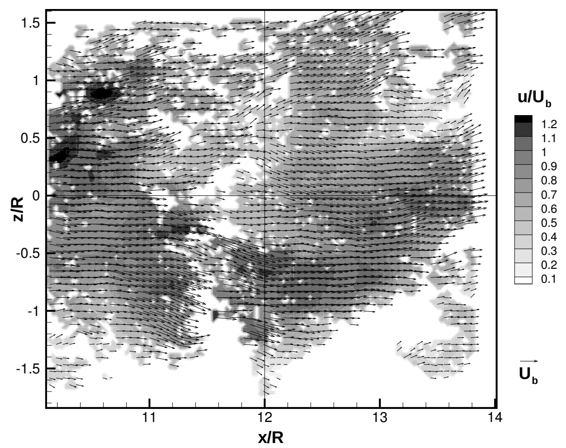

Figure 11: Instantaneous velocity field in xz-plane at $y = 0$ and contours of u. $S = 0.43$. Same field as in Fig. 10.

in a random fashion. The high-speed core of the jet tends to quickly shift, stretch and deform. Hence, the counter-rotating core region of the swirling jet seems to be affected mostly by the large sweeping motions. No other coherent pattern has been identified that would be specific to that flow region.

In the case of a pipe jet, as opposed to a smooth contraction jet, Mi et al. (2001) and Xu and Antonia (2002) have found that the regular formation of vortex rings resulting from the shear layer instability is disrupted by turbulent exit conditions. Moreover, the initially thicker shear layer in the case of the pipe jet results in longer wavelength primary instabilities and structures and delays their onset. To see if large-scale azimuthal vortices occur in the present swirling jet, the instantaneous velocity fields in the xz-plane were analyzed via Galilean decomposition with a constant advection velocity of $0.6U_b$ removed. This velocity is expected to be close to the average convection velocity of the large-scale vortical structures. No significant qualitative differences were observed when changing the advection velocity in the range 0.5-$0.7U_b$.

Large-scale vortical motions are clearly present in the swirling jet in the region around $x/D = 6$. As an example, Fig. 12 shows a case where at least six vortical motions can

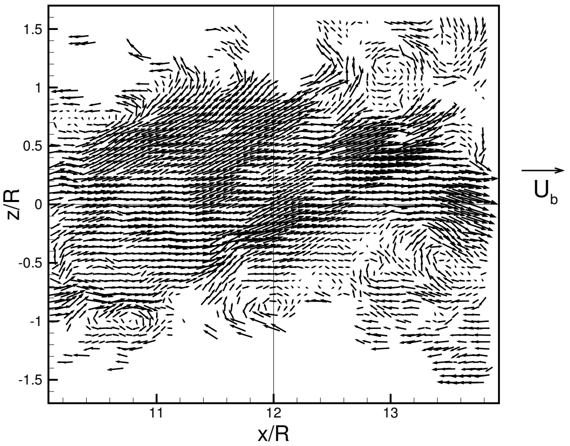

Figure 12: Instantaneous velocity field in xz-plane at $y = 0$. $S = 0.43$. Galilean decomposition with $U_c = 0.6U_b$.

be identified (three at the upper edge and three at the lower one). Velocity vectors in these regions are unfortunately often rejected or false due to the lack of seeding at the edges of the measured portion of the flow field, $|r/R| \approx 1$. The large vortical motions are also often only partially captured at these edges. For these reasons, they are more easily identified with the animation of the velocity fields than with still images.

The large-scale vortices are generally located at $r/R > 0.5$, which is consistent with the location of the shear layer upstream. They usually appear together with the large-scale sweeping motions previously discussed. As is the case in Fig. 12 at $x/R \approx 10.6$, they sometimes occur in counter-rotating pairs roughly aligned in the radial direction, with a vortex on each side of the centerline. Such counter-rotating vortex pairs could be closed or broken remnants of vortex rings. A jet of high momentum fluid is usually present in between the large-scale counter-rotating vortices. The axial velocity spectra obtained by Facciolo (2006) suggest that the interaction and breakdown of the primary vortical structures is clearly underway at $x/D = 6$ for both the swirling and non-swirling jets. By studying the contours of $-\partial u/\partial r$ in the yz-plane, closed loops of $-\partial u/\partial r > 0$ (probable positive azimuthal vorticity) were never identified but broken arches with a radius of $r \approx 0.5D$ appear frequently, especially for the non-swirling jet.

In the case of the non-swirling jet, vortical motions are the dominant feature observed in the yz-plane (PIV data in the xz-plane is not available). The high-speed core of the jet does not meander like in the swirling jet flow. Streamwise vortices concentrated along a centered ring band are sometimes found (see Fig. 8), where the radius of the ring is approximately equal to the pipe radius R. These vortices could be the remnants of streamwise braids generated upstream as secondary shear layer instabilities. The lack of regularity in the occurence and the shape of these rings of streamwise vorticity may be reinforced by the fact that the initial conditions of the jet are those of a turbulent pipe flow, as opposed to a thin laminar shear layer in the case of a smooth contraction jet flow. The rings of streamwise vortices were not observed in the swirling jet, suggesting their absence or an earlier onset of the strong nonlinear interactions in the flow field. In the swirling jet, the streamwise vortices are located everywhere in the jet in a more random fashion. They are however more present in and around the highly deformed jet core as is the case in Fig. 9, where the high-speed core forms a large diagonal band. The large-scale vortices are typically of the same size and strength in both the non-swirling and swirling jets. In the swirling jet, they are smaller than the large sweeping motions previously discussed and they can even be imbedded in them (Fig. 9).

CONCLUSIONS

We present PIV data for all six Reynolds stress components for turbulent jets with and without swirl at $x/D = 6$. It is clear that the swirl increases the turbulence intensities in the jet significantly. The budget for the angular momentum density shows that the radial turbulent transport is large and likely is the cause for the counter rotating core.

The time-resolved PIV data show that the swirling jet is dominated by violent, large-scale sweeping motions that are not present at such a scale and strength in the non-swirling jet. The strong sweeping motions often come together with a waviness of the jet. Under their presence, the high-speed core of the jet tends to quickly shift, stretch and deform. These sweeping motions are often linked to the presence of large-scale azimuthal vortices. The latter are probably the remnants of the vortex rings formed upstream by the shear layer instability.

Counter-rotation of the core of the swirling jet was not found to be due to turbulent structures specific to the core region. It appears to be simply due to the fact that the large-scale turbulent motions, which often lead to strong $u'_\theta u'_r$, are efficient in transporting mean angular momentum radially outward.

ACKNOWLEDGEMENT

The development of rotating pipe facility and most of the measurements were sponsored by STEM, the Swedish Energy Agency. Part of this work was carried out when YM was on a research visit to KTH in the summer of 2006, which was partly sponsored through STINT, The Swedish Foundation for International Cooperation in Research and Higher Education. Financial support from NSERC of Canada is gratefully acknowledged by YM.

REFERENCES

Facciolo, L., and Alfredsson, P.H., 2004, "The counter-rotating core of a swirling turbulent jet issued from a rotating pipe flow". *Phys. Fluids* **16**, L71–L73.

Facciolo, L., 2006, "A study on axially rotating pipe and swirling jet flows". PhD thesis, Royal Institute of Technology, Stockholm, Sweden.

Facciolo, L., Tillmark, N., Talamelli, A., and Alfredsson, P.H., 2007, "A study of swirling turbulent pipe and jet flows". *Phys. Fluids* **19**, 035105.

Mi, J., Nobes, D.S., and Nathan, G.J. 2001, "Influence of jet exit conditions on the passive scalar field of an axisymmetric free jet". *J. Fluid Mech.* **432**, 91–125.

Xu, G., and Antonia, R.A. 2002, " Effect of different initial conditions on a turbulent round free jet". *Exp. Fluids* **33**, 677–683.